Journal of Applied Physics

RESEARCH ARTICLE | AUGUST 22 2023

Modeling multi-site emission in porous electrosprays resulting from variable electric field and meniscus size

C. B. Whittaker ; B. A. Jorns

Journal of Applied Physics 134, 083301 (2023)
https://doi.org/10.1063/5.0159396

Journal of Applied Physics ARTICLE pubs.aip.org/aip/jap

Modeling multi-site emission in porous electrosprays resulting from variable electric field and meniscus size

Cite as: J. Appl. Phys. **134**, 083301 (2023); doi: 10.1063/5.0159396
Submitted: 23 May 2023 · Accepted: 19 July 2023 ·
Published Online: 22 August 2023

View Online Export Citation CrossMark

C. B. Whittaker[a)] and B. A. Jorns

AFFILIATIONS

Department of Aerospace Engineering, University of Michigan, Ann Arbor, Michigan 48109, USA

[a)]**Author to whom correspondence should be addressed:** cbwhitt@umich.edu

ABSTRACT

A model predicting the number of emission sites and total current from a porous conical electrospray emitter as functions of voltage is derived. A pressure balance between capillary and electric forces is used to determine an onset criterion for individual menisci, and an ionic emission scaling law is invoked to predict the current each meniscus emits. These submodels are integrated over a phenomenological meniscus size distribution and the area of the emitter to yield a model for emitter performance as a function of five free parameters, two for the ionic emission submodel and three for the meniscus size distribution. Bayesian inference is applied to determine these model parameters from an existing dataset [Dressler *et al.*, J. Propul. Power **38**, 809 (2022)]. The model predictions after training are compared to the experimental data, and it is found that the majority of the data are within a 90% credible interval. The ability of the model to capture key trends in the experimental data is attributed to the interplay of two effects: the distribution over meniscus size on the emitter and the position-dependent electric field. The calibrated model results also suggest that the emitter surface is wetted by a series of large but sparsely distributed pools of propellant. The performance and extensibility of the model are examined within the context of model-based design for porous electrospray array thrusters.

I. INTRODUCTION

The onset of multiple emission sites in porous electrospray thrusters is a poorly understood phenomenon intrinsically linked to the operation of these in-space propulsion devices. Electrosprays produce energetic beams of charged particles by subjecting a conducting liquid to a strong electric field. This field induces deformation of the electrified fluid meniscus into a Taylor cone structure;[1] at the apex of this structure, charge is extracted through either an electrohydrodynamic jet[2] or electrokinetic evaporation of ions from the liquid bulk.[3] These mechanisms make electrosprays attractive as a form of in-space electric propulsion, as they support high thrust per weight and per area, and they avoid the volume-to-area losses associated with plasma-based propulsion systems like gridded ion engines and Hall thrusters.[4] While all electrospray propulsion implementations adopt a sharp emitter geometry to amplify the field at the tip and reduce the operational voltage necessary to produce Taylor cones, they differ in how fluid is delivered to this region, whether by capillary tubes,[5,6] along a roughened exterior,[7] or through a porous medium.[8,9]

Porous media-based systems have become increasingly favored for propulsive applications for their machinability[9,10] and ability to access the pure ionic emission regime (an operating mode characterized by high specific impulse).[11,12] As documented extensively, however, these emitters are particularly prone to the onset of multiple emission sites with increasing voltage,[11,13–19] whereby multiple Taylor cones can form on a single emitter and produce distinct beamlets. Indeed, porous wedge architectures rely on such multi-site emission.[20–23] This behavior can be problematic, as secondary emission sites often produce beams at angles off the nominal thrust axis. In addition to reducing system efficiency through corresponding divergence losses, such wide-angle beams are also more likely to deposit propellant on downstream electrodes, encouraging arcing between electrodes, and reducing system lifetimes.[15,24,25] This problem is compounded when considering aggregated systems of many emitters, i.e., "electrospray array thrusters," which are often necessary to achieve sufficient thrust for in-space applications.[4] For example, emitter-to-emitter variability stemming from finite manufacturing and assembly tolerances can precipitously decrease expected lifetimes.[26] Understanding multi-site emission is thus imperative for predicting device performance at scale.

With this challenge in mind, there have been previous efforts to investigate and predict this phenomenon. Wright and Wirz,[27] for example, postulated that a periodic internal pressure distribution could lead to the formation of multiple Taylor cones in porous wedge systems. Dressler *et al.*,[16] on the other hand, considered the hypothesis that multi-site emission can be explained by variability in meniscus size on the substrate. Mensici of different sizes have varying capillary pressures to resist onset, and additional sites will activate as the available electric pressure (a function of voltage) increases. This latter interpretation is particularly physically plausible given the stochastic structure of the substrate and the wetting properties of ionic liquids. Ultimately, while both of these approaches were able to match some aspects of experimental data, the deleterious effects of multi-site emission on device performance warrant continued and rigorous model refinement.

To this end, in this work, we adopt a similar hypothesis as Dressler *et al.* and expand on this previous study by adding fidelity in two key ways. First, determining the actual distribution of menisci on substrates experimentally has proved to be prohibitively difficult to date. We have thus developed a generalizable description for this distribution with parameters that can be learned formally from experimental data. Second, we propose a new mechanism for multi-site emission related to the geometry of the emitter. In practice, the sharp geometries of these devices produce electric fields that are strong functions of position. As a result, menisci in regions of weaker field like the sides of an emitter will require higher voltages to activate compared to those at the emitter apex, where the field is strongest. This effect is ultimately convolved with the influence of the meniscus size distribution.

This paper is organized as follows. In Sec. II, we derive models for the number of emission sites and emitted current as a function of voltage. In Sec. III, we outline our methodologies for training the models from data and describe the dataset used to train them. In Sec. IV, we present the results of our model inference, showing model predictions subject to uncertainty in the model parameters and giving distributions over the parameters themselves. Finally, in Sec. V, we discuss our results, first interpreting them physically and then examining our modeling strategy as relates to the design of electrospray arrays.

II. MODEL

The electrospray emitters considered here operate by biasing a porous substrate infused with an ionic liquid propellant to high voltage with respect to an extraction electrode. The geometry of the emitter serves to amplify the electric field and provide fluidic conduction from a nearby reservoir. This produces a population of electrically stressed menisci at the surface of the substrate, which deform into structures—Taylor cones—which evaporate charge. In space propulsion applications, this beam of particles is used to produce thrust, and charge neutrality must be maintained by alternating the polarity of the extraction process or through an external cathode.[4]

We derive in this section a model predicting the number of sites and total emitted current of a porous electrospray emitter. We first parameterize the emitter geometry and propose a phenomenological model for the density of menisci on the emitter surface. We then present component models that describe the onset of individual emission sites, the current emitted by each site, the hydraulic impedance of the emitter, and the electric field at its surface. We conclude by integrating these sub-models over the area of the emitter to determine the bulk emission behavior.

A. Emitter geometry

We consider here emission from porous conical emitters, whose geometry we approximate as a spherically capped cone (Fig. 1). The body of the cone has half-angle α, and the radius of the cap is given by R_c. The total height of the emitter is denoted by h. We also specify the geometry of the extraction electrode, which is shown alongside that of the emitter in Fig. 1. The extractor acts as a terminus for the voltage while providing apertures through which the beam can escape. We model this element as an equipotential sheet of thickness t_e which is offset from the apex of the emitter by the distance d and perforated by a circular aperture of radius R_A.

Given the axisymmetry of the cone geometry, we elect to use the arc length along the cone section, s, to parameterize the surface, where $s = 0$ is at the emitter apex. We, in turn, represent the surface area of the cone as differential annular segments along its cross section (Fig. 1). Within our parameterization, $\mathrm{d}A = \frac{\mathrm{d}A}{\mathrm{d}s}\mathrm{d}s$, where

$$\frac{\mathrm{d}A}{\mathrm{d}s} = \begin{cases} 2\pi R_C \sin(s/R_c), & s \in \left[0,\ \left(\frac{\pi}{2}-\alpha\right)R_c\right], \\ 2\pi\left[R_c\cos\alpha + \left(s - \left(\frac{\pi}{2}-\alpha\right)R_c\right)\sin\alpha\right], & s \in \left[\left(\frac{\pi}{2}-\alpha\right)R_c,\ \left(\frac{\pi}{2}-\alpha\right)R_c + (h - R_c(1-\sin\alpha))\sec\alpha\right]. \end{cases} \tag{1}$$

Physically, this expression represents the separation of the cone into two domains: the spherical cap for smaller values of s and the conical body of the cone for larger values. The differential area contained in an annulus increases with increasing arc length in both cases.

B. Meniscus population

The porous medium is an interconnected network of fluidic pathways that terminate at the surface of the substrate, where the pooling liquid interfaces with vacuum and forms a collection of menisci which represent possible sites for emission. It is intuitive to link the distribution of menisci present on the emitter tip directly to the pores of the underlying substrate. However, characterizations of these pores often arise as abstractions of the bulk fluidics of the substrate, usually approximating its structure as a bundle of parallel capillary tubes. While such an approximation often provides useful information about the constrictions that form within the substrate and is a key metric for filtration applications, it is ill-posed as an

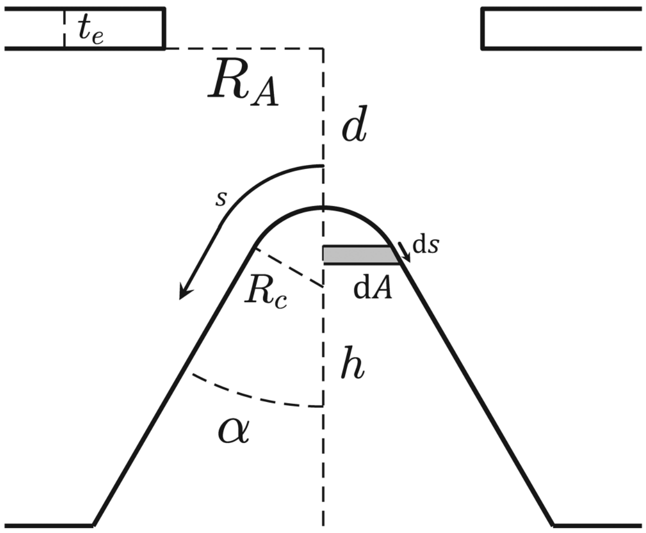

FIG. 1. Spherically capped cone dimensions and parameterization.

indicator for the detailed microscopic pore structure.[28] In practice, the menisci arise from the complex interplay of the substrate porosity with the wetting properties of the material and fluidic boundary conditions. Indeed, previous work suggests that some pooling of the menisci—such that their sizes are larger than the characteristic pore size—is necessary to capture emission behavior, especially for emission onset.[16,29,30]

To avoid the complexity of modeling this detailed interaction, we develop here a probabilistic treatment for the distribution of menisci on the emitter surface. To this end, we assume menisci take a range of diameters, p, governed by a density function, $f(p)$, where $f(p)\,\mathrm{d}p$ is the differential proportion of menisci with diameter p. This distribution encodes the variability or uncertainty in the size of an emission site, which partially determines its emission properties. We can describe bulk properties of the population of menisci by taking moments over $f(p)$. For example, the mean area of a meniscus on the emitter is $\bar{A}_p = \int \frac{\pi}{4} p^2 f(p)\,\mathrm{d}p$.

By further integrating these moments over the area of the emitter, we determine its aggregate properties,

$$A = \int \mathrm{d}A, \quad N_p = \int n_p\,\mathrm{d}A, \quad A_m = \int \bar{A}_p\, n_p\,\mathrm{d}A, \quad n_p = \frac{\psi}{\bar{A}_p}. \tag{2}$$

We have defined here the total area of the emitter, A, the total number of menisci on the emitter, N_p, the total surface area covered by menisci, A_m, and the number density of menisci, n_p. In defining n_p, we have introduced the scaling factor $\psi = \frac{A_m}{A} \in [0, 1]$, the surface wetting coefficient, which represents the proportion of the surface composed of menisci (i.e., covered in liquid).

To facilitate our analysis, we propose a phenomenological form for the meniscus diameter distribution, $f(p)$,

$$f(p) = \begin{cases} \frac{1-m}{p_2^{1-m} - p_1^{1-m}} \frac{1}{p^m}, & p \in [p_1, p_2], \\ 0, & \text{otherwise}. \end{cases} \tag{3}$$

This distributes the menisci over sizes between some minimum diameter p_1 and some maximum diameter p_2, such that the number density is inversely proportional to feature size with a characteristic meniscus exponent, m. The first fraction is simply a normalizing constant. Physically, this distribution represents a packing of the surface where smaller menisci fit in the spaces between larger menisci, a phenomenon also observed in beading on hydrophillic surfaces.[31] In practice, Eq. (3) is expedient because it admits tractable moments. For example, the mean area of a meniscus is

$$\bar{A}_p = \frac{\pi}{4} \frac{1-m}{p_2^{1-m} - p_1^{1-m}} \frac{p_2^{3-m} - p_1^{3-m}}{3-m}. \tag{4}$$

Finally, while in general $f(p)$ could be considered a position-dependent quantity [i.e., $f(p, s)$], we take it to be uniform over the emitter.

C. Onset criterion

We now formulate a model for when menisci across the body of the emitter develop into Taylor-cone structures and shed charge. To do so, we define an indicator function for some onset criterion for emission, 1_O. This function has a value unity when the onset criterion is satisfied (indicating formation of a Taylor cone) and a value zero otherwise. The number of active emission sites on the emitter, N_s, is thus

$$N_s = \iint 1_O(p, E(s)) f(p)\,\mathrm{d}p\; n_p \frac{\mathrm{d}A}{\mathrm{d}s}\,\mathrm{d}s. \tag{5}$$

The moment $\bar{1}_O(E(s)) = \int 1_O(p, E(s)) f(p)\,\mathrm{d}p \in [0, 1]$ is the mean number of emission sites per meniscus, or the proportion of menisci which have onset. This is then integrated over the emitter area and scaled by the meniscus density—similarly to N_p in Eq. (2)—to yield the number of sites. We have noted explicitly here that 1_O is a function of p, the meniscus size, and $E(s)$, the local electric field magnitude, where $E(s)$ is itself a function of position on the emitter.

To obtain an onset criterion for the indicator function, we begin, after Martinez-Sanchez,[32] by examining the pressure balance

$$\frac{1}{2}\varepsilon_0 E(s)^2 \geq b_0 P_c. \tag{6}$$

Here, the left hand side represents electric pressure provided by the applied field, where ε_0 is the permittivity of free space. The right hand side represents the force from surface tension as some proportion, $b_0 > 0$, of the characteristic capillary pressure of the meniscus, $P_c = \frac{4\gamma}{p}$, where γ is the surface tension of the liquid. Physically, Eq. (6) shows that when the applied electric stress exceeds the restoring force from capillary pressure, the meniscus deforms into a Taylor cone and begins to emit charge.

While Eq. (6) has been applied to capture key trends in onset behavior experimentally, recent work has suggested that it should be modified to include the effect of reservoir pressure, P_r, which is a boundary condition for the flow feeding into the emitter.[3,20,27,33–35] To represent this analytically, we adopt a modified form of Eq. (6),

$$\frac{1}{2}\varepsilon_0 E(s)^2 \geq b_0 P_c - b_1 P_r. \tag{7}$$

Again, we have some proportionality, $b_1 > 0$, and this expression captures the fact that reservoir pressure reduces the required electric field when positive or provides additional restoring force when negative. The latter is most often the case in passively fed systems.[3,20,27] We further simplify Eq. (7) by linearizing under the assumption that the reservoir pressure contribution is small compared to the surface tension effect,

$$\sqrt{\frac{1}{2}\varepsilon_0}E(s) \geq \beta_0\sqrt{\frac{4\gamma}{p}} - \beta_1\frac{P_r}{\sqrt{\frac{4\gamma}{p}}} = \sqrt{\frac{1}{2}\varepsilon_0}E_0, \tag{8}$$

where we have substituted for the characteristic capillary pressure and collapsed the proportionalities into the parameters $\beta_0 > 0$ and $\beta_1 > 0$, which modulate the relative influence of the capillary and reservoir pressure forces. In Secs. III–V, we leverage results from previously reported simulations to infer the values of these coefficients and justify our linearization *a posteriori*. As a shorthand, we have additionally adopted the notation $E_0 = E_0(p)$ for the onset field strength, the value of E where the inequality of Eq. (8) is exactly satisfied.

As a final step, we leverage this criterion to provide a piecewise definition of the indicator function,

$$1_O(p, E(s)) = \begin{cases} 1, & E(s) \geq E_0(p), \\ 0, & \text{otherwise.} \end{cases} \tag{9}$$

It follows from Eq. (8) that for a fixed surface tension and electric field magnitude, the onset criterion is only satisfied over some finite interval of meniscus diameter, $p \in [p_{O,1}, p_{O,2}] \subseteq [p_1, p_2]$. The moment $\bar{1}_O(E(s))$ is defined over this interval, yielding

$$\bar{1}_O(E(s)) = \frac{p_{O,1}^{1-m} - p_{O,2}^{1-m}}{p_1^{1-m} - p_2^{1-m}}. \tag{10}$$

A procedure for computing $p_{O,1}$ and $p_{O,2}$ appears in the Appendix.

D. Current emission

Having formulated a model for the onset of emission sites on the emitter, we now develop an expression for the current sourced by these sites, both individually and in aggregate. We begin by assuming that only the active sites [those satisfying Eq. (8)] can emit current, and we generically denote the current emitting from a single active site as $i(p, E(s))$. We again include functional dependencies on p and $E(s)$ explicitly. To motivate an expression for this current, we consider emitters sourcing solely (or near solely) ionic species—that is, operating in a pure ionic regime. We justify this assumption in light of previous work that has shown porous conical emitters facilitate ionic emission.[9,11,15]

We model this ionic current by invoking a scaling law for ionic emission originally presented in the numerical investigations of Coffman[3,34] and later examined by Gallud-Cidoncha.[30,35] In those works, they considered a prototypical meniscus immersed in a uniform background field and related the current emitted from the site to the fluid flow driven by pressure,

$$i(p, E(s)) = \xi\rho\frac{\Delta P}{r_h}. \tag{11}$$

In Eq. (11), the driving pressure, ΔP, acts to create a volumetric flow rate of viscous propellant, $\frac{\Delta P}{r_h}$, where r_h is the hydraulic impedance to the emission site. This volumetric flow rate is then dimensionally transformed to current through the mean charge-to-mass ratio of the beam, ξ, and the fluid density, ρ. The driving pressure is some function, ζ, of the electric field at the meniscus, $\Delta P = \zeta(E(s))$. Following Refs. 3, 34, and 35, we linearly expand this dependence about the onset field, E_0, yielding

$$i(p, E(s)) = \frac{\xi\rho}{r_h}\left[\zeta(E_0) + \frac{\mathrm{d}\zeta}{\mathrm{d}E}(E_0)(E(s) - E_0)\right] \tag{12}$$

$$= \frac{\xi\rho}{r_h}\left[\zeta_0\frac{4\gamma}{p} + \zeta_1\sqrt{\frac{4\gamma}{p}}\sqrt{\frac{1}{2}\varepsilon_0}(E(s) - E_0)\right]. \tag{13}$$

In Eq. (13), we have collected the expansion terms into the dimensionless model parameters ζ_0 and $\zeta_1 > 0$, which Coffman *et al.* argue should be universal properties of ionic sprays.[3]

Equation (13) then permits, similarly to Eq. (5), computation of the total current sourced by the emitter as

$$I = \iint i(p, E(s))\, 1_O(p, E(s))\, f(p)\, \mathrm{d}p\; n_p\frac{\mathrm{d}A}{\mathrm{d}s}\,\mathrm{d}s. \tag{14}$$

The moment $\bar{i}(E(s)) = \int i(p, E(s))\, 1_O(p, E(s))\, f(p)\, \mathrm{d}p$ admits an analytical expression for the mean current per emission site,

$$\begin{aligned}\bar{i}(E(s)) = \frac{\rho\xi}{r_h}\frac{p_2 p_1}{p_2 - p_1}\Bigg[&4\gamma(\zeta_0 - \zeta_1\beta_0)\frac{p_{I,1}^{-m} - p_{I,2}^{-m}}{m} \\ &+ \sqrt{2\gamma\varepsilon_0}\zeta_1 E(s)\frac{p_{I,1}^{\frac{1}{2}-m} - p_{I,2}^{\frac{1}{2}-m}}{m - \frac{1}{2}} \\ &+ \zeta_1\beta_1 P_r\frac{p_{I,1}^{1-m} - p_{I,2}^{1-m}}{m - 1}\Bigg].\end{aligned} \tag{15}$$

This moment is defined over some interval $p \in [p_{I,1}, p_{I,2}] \subseteq [p_{O,1}, p_{O,2}] \subseteq [p_1, p_2]$ for which Eq. (13) is non-negative and the onset criterion [Eq. (8)] is satisfied. It is the case that $p_{I,\{1,2\}} \equiv p_{O,\{1,2\}}$ because for negative values of ζ_0 the current magnitude, i, would be negative in certain regions of p-$E(s)$ space, which is non-physical. This is a consequence of linearizing the pressure dependency in Eq. (12). Practically, the moment must be truncated to exclude these regions. An algorithm for computing $p_{I,1}$ and $p_{I,2}$ appears in the Appendix.

E. Hydraulic impedance

The preceding current model requires an estimate for the hydraulic impedance to the emission site, r_h. We do so by taking a parallel sum over all active sites,

$$\frac{1}{R_h} = \frac{N_s}{r_h} = \iint \frac{1}{r_h} 1_O(p, E(s)) f(p)\, \mathrm{d}p \, \frac{\mathrm{d}A}{\mathrm{d}s} \, \mathrm{d}s, \tag{16}$$

where we have implicitly approximated the hydraulic impedance to each site as equal. The total hydraulic impedance across all active sites, R_h, we treat as the conical emitter impedance of Courtney,[13]

$$R_h = \left(\frac{\mu}{2\pi\kappa} \frac{1}{1-\cos\alpha} \left[\frac{\tan\alpha}{R_c} - \frac{\cos\alpha}{h + R_c(\csc\alpha - 1)} \right] \right), \tag{17}$$

where κ is the permeability of the substrate and μ is the dynamic viscosity of the fluid.

F. Field magnitude

The final outstanding component of the model is the determination of the electric field magnitude as a function of position on the emitter surface, $E(s)$. We note that Taylor cone structures produced at the emission sites by the action of the applied electric field will locally modify it. However, it is common treatment to define $E(s)$ as the field in the absence of this perturbation,[3,34,35] such that it is computed considering only the geometry of Fig. 1. To this end, we approximate the emitter surface (see Sec. II A) as equipotential and numerically solve Gauss's law in vacuum, $\nabla^2\phi = 0$. Here, ϕ is the electrostatic potential, $\vec{E} = \nabla\phi$, and we have ignored the effect of the small space charge of the beam.[34,36] When we implement the numerical solution, we assume the emitter is held at a potential $\phi_{em} = V$ relative to the extractor. The resulting solution for the electric field, $E(s)$, depends on position, but the overall magnitude is linearly proportional to V. We thus solve the model once for a reference voltage of 1 V and scale as needed to model other operating voltages. With this invocation of an electrostatic solver to compute $E(s)$, the multi-site emission model is now complete. We work in Sec. III to regress this model against experimental data.

III. MODEL INFERENCE

While the preceding model is informed from first principles, it contains several parameters that are not known *a priori*, for example, ζ_0 and ζ_1 in Eq. (13). These parameters arise as macroscopic approximations to the detailed physics not captured with our reduced fidelity approach. Correspondingly, these parameters must be inferred from experimental data (i.e., model fitting). Once we have calibrated the model against training data, we can then assess the model's ability to capture observed trends (i.e., goodness of fit) and derive physical insights.

To determine these unknown model parameters, we require some means of regressing them from experimental data. A common approach is a least squares fit, but this fails to account rigorously for uncertainty in experimental data or, more crucially, uncertainty in the model parameters used to represent the simplified physics. We, therefore, adopt a Bayesian approach to inference, wherein we represent the model parameters as probabilistic.

In this section, we first detail the experimental data used as a training set. This is followed by a description of the model inputs and outputs. We finally present the prescription for performing Bayesian inference to determine probability distributions for the model parameters given the experimental data.

A. Experimental data set

Multi-site emission is an active area of investigation in porous electrosprays.[14,16,22,23,37] We consider here the experiments of Dressler *et al.*[16] They operated a pair of porous conical electrospray emitters made from P5 grade borosilicate glass frit on the ionic liquid 1-ethyl-3-methylimidazolium-bis(trifluoromethylsulfonyl) imide (EMI-TFSI). Propellant was supplied to the emitters from a reservoir made of P3 glass frit. The emitters were operated in parallel, sharing an extraction electrode and effectively forming a small electrospray array. Over a range of operating voltages, a micro-Faraday probe was swept through the combined emitter plume to resolve the beamlets produced by individual emission sites. A separate current monitor was also used to measure the combined emission current of the two emitters. To estimate the number of sites and current produced by each emitter from these joint measurements, the authors divided the domain into two and assumed emission within each half was produced solely by the emitter in that half (cf. Ref. 16). As a training data set, we take results for their "Tip 2" (see Fig. 2) operating in the positive emission mode. We give the corresponding number of active sites, N_s, and emitter current, I, as taken from Ref. 16, in Table I.

B. Model parameters and outputs

Table II shows the key outputs and inputs for the multi-site emission model presented in Sec. II. The outputs of interest for this work are the number of active sites, N_s, and the total emitter current, I. There are several inputs to the model, including the voltage of the emitter, V, the scaling coefficients, $(\beta_0, \beta_1, \zeta_0, \zeta_1)$, the surface wetting parameters, (ψ, p_1, p_2, m), the substrate fluidic properties, (κ, P_r), the propellant properties, (γ, ρ, μ), the charge to mass ratio of the beam, ξ, and the device geometry, $(R_c, h, \alpha, d, R_A, t_e)$.

We assume as given several of these input parameters, leveraging the geometry of the emitters provided in Ref. 16 for the training data set as well as published properties of the substrate and propellant. For the permeability of the emitter substrate, we use the value quoted by the substrate manufacturer (ROBU Glasfilter-Geräte GmbH, see Refs. 16 and 38). We estimate the reservoir pressure as $P_r = -\frac{4\gamma}{p_{\max}}$, where $p_{\max}$ is the maximum through-pore size in the reservoir substrate (40 μm for P3 grade). We take the minimum meniscus size, p_1, to be equal to the minimum through-pore size of the emitter substrate, 1 μm for P5 frit. The fluid properties of Table II are calculated for EMI-TFSI assuming a temperature of 295 K using the Electrospray Propulsion Engineering Toolkit

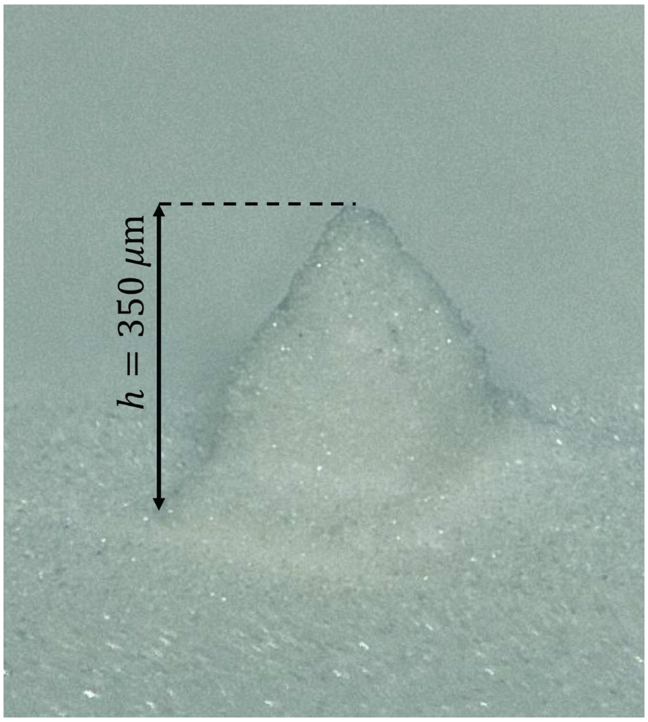

FIG. 2. Photo of the "Tip 2" emitter of Ref. 16, printed with permission; emitter height, h, indicated for scale.

(ESPET) propellant database, which is built into the ESPET web app.[29,39] The charge-to-mass ratio we take from time-of-flight mass spectrometry measurements also reported in Ref. 16 for the same emitters (positive mode, focusing lens on). This value was shown to vary within 5% as a function of discharge voltage, and so we use an average value as representative of all voltages.

TABLE I. Experimentally measured number of sites, N_s, and emitter current, I, for "Tip 2" of Ref. 16 as a function of emitter voltage, V, in the positive emission mode.

Voltage (V)	Number of sites	Emitter current (μA)
1100	1	0.01
1200	1	0.04
1300	2	0.11
1400	2	0.37
1500	4	0.91
1550	4	1.18
1600	4	1.59
1700	4	1.63
1800	6	2.54
1900	8	3.10
2000	9	3.65

TABLE II. Inputs and outputs of the multi-site emission model.

Input	Description	Value
β_0	Capillary pressure coefficient	0.519
β_1	Reservoir pressure coefficient	0.400
ζ_0	Ionic emission offset	Uncertain
ζ_1	Ionic emission slope	Uncertain
ψ	Surface wetting coefficient	Uncertain
p_1	Minimum meniscus size	1.0×10^{-6} m
p_2	Maximum meniscus size	Uncertain
m	Meniscus exponent	Uncertain
κ	Substrate permeability	151×10^{-15} m^{-2}
P_r	Reservoir pressure	−3511 Pa
γ	Surface tension	35.11×10^{-3} N m^{-1}
ρ	Density	1522 kg m^{-3}
μ	Dynamic viscosity	33.94×10^{-3} Pa s
ξ	Charge-to-mass ratio	217×10^{3} C kg^{-1}
R_c	Tip radius of curvature	16×10^{-6} m
h	Emitter height	350×10^{-6} m
α	Cone half angle	30 deg
d	Electrode gap distance	0 m
R_A	Aperture radius	175×10^{-6} m
t_e	Extractor thickness	70×10^{-6} m
Output	**Description**	
N_s	Number of active emission sites	
I	Total emitter current	

We use the device geometries as reported in Ref. 16 with a few modifications. We note here that unlike in our idealized geometry (Fig. 1), the actual emitter (Fig. 2) was not conical through its full height. However, near the apex where most emission is expected, it is nearly so, and we thus neglect the impact of these non-idealities on our model predictions. Similarly, the extractor electrode in the reference had a slotted geometry, which is a departure from the axisymmetric geometry shown in Fig. 1. This serves to produce an electric field that is weaker across the emitter and inhomogeneous about its circumference. To capture these effects, we rely on a 3d electrostatic simulation of the slotted geometry done using COMSOL Multiphysics' AC/DC module. In this case, the "aperture radius" of Table II instead denotes the half-width of the slot. From this simulation, we extract an $E(s)$ that is an average of the field profiles on the cross sections of the emitter parallel and orthogonal to the slot, which we then use for the 1d treatment of Eqs. (5) and (14). We show the resulting averaged field profile in Fig. 3 as a solid black line, and the two constituent profiles in dashed gray. As is evident in the figure, the field is strongest at the apex of the emitter and drops precipitously beyond the emitter tip, with the vertical line of Fig. 3 being the s position at the edge of the spherical cap of the model geometry. As we find the two profiles differ within 1% over this region, we expect taking their average to be a good approximation.

For the onset parameters β_0 and β_1, we refer to the results of Ref. 34, where this dependence was interrogated numerically within

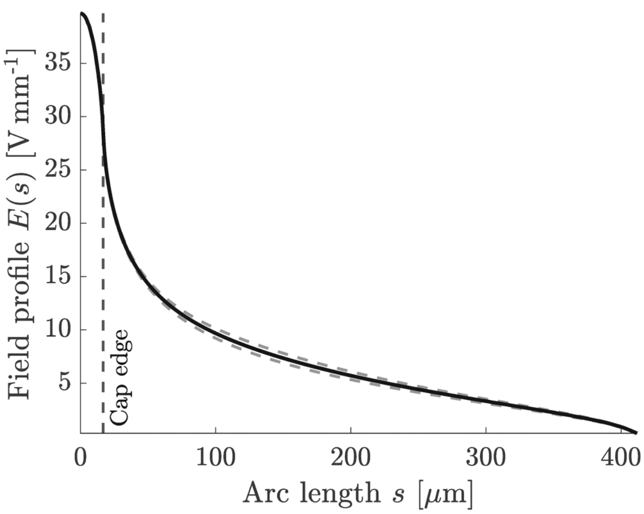

FIG. 3. Modeled electric field profile $E(s)$ (solid black) as a function of s for the porous conical emitter of Ref. 16; the profile is averaged over two orthogonal cross sections of the emitter (each in dashed gray) and computed for $V = 1$ V; the vertical line is coincident with the edge of the spherical cap.

the dimensionless space of

$$\hat{E}_0 = E_0 \left(\sqrt{\frac{8\gamma}{\varepsilon_0 p}}\right)^{-1}, \quad \hat{P}_r = P_r \left(\frac{4\gamma}{p}\right)^{-1}. \tag{18}$$

In Fig. 4, we display the data of Ref. 34 as a function of $\hat{P}_r$, along with a least squares fit of Eq. (8) to the data. We take these best-fit values as our values for β_0 and β_1. We will justify *a posteriori* that this range of $\hat{P}_r$ is representative of the system of interest. We also note that while there is error inherent in this model from simplifying the physics to this linear description, the goodness of fit evident in the figure indicates such error would be small on the scale of the problem.

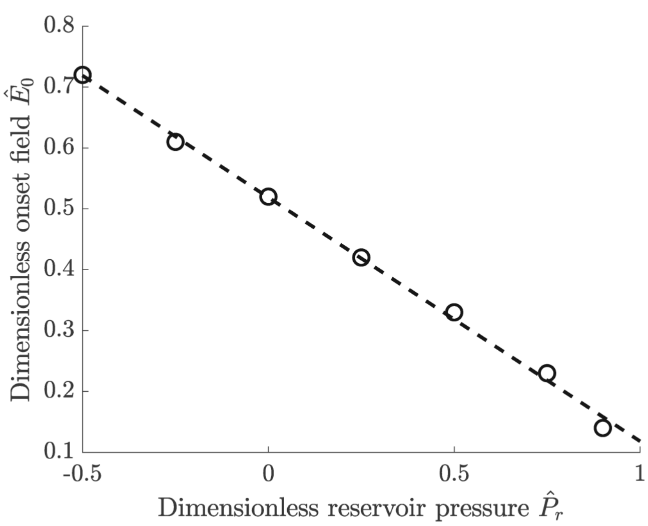

FIG. 4. Least squares fit (dashed line) of Eq. (8) to simulations of Coffman *et al.*[34] (circles).

This leaves the current emission model parameters ζ_0 and ζ_1, the surface wetting coefficient, ψ, the maximum meniscus size on the surface, p_2, and the meniscus distribution exponent, m, as uncertain. We collect these parameters as $\theta = (\zeta_0, \zeta_1, \psi, p_2, m)$, and we ultimately elect to infer these parameters from experimental data. We discuss this procedure in Sec. III C.

C. Bayesian regression

We can now turn our attention to inferring the unknown model parameters of the previous section from the experimental data described in Sec. III A. The number of sites and current of the source in Ref. 16 were obtained concurrently at N_d different voltages. Thus, we have a set of N_d training data, $X = \{x^{(k)}\} = \{x^{(1)}, x^{(2)}, \ldots, x^{(N_d)}\}$, where $x^{(k)} = (V^{(k)}, N_s^{(k)}, I^{(k)})$ and $k = 1, 2, \ldots, N_d$ is an index for the data. We augment the reported data of Table I with an additional null datum, $x^{(0)} = (1000\,\text{V}, 0\,\text{sites}, 0\,\mu\text{A})$. This addition is consistent with the observation[16] that below 1100 V, there are no active sites and no emission current.

We seek to learn the model parameters, θ, from this dataset. To do so within a Bayesian context, we compute the posterior probability, $\mathrm{P}(\theta \mid X) \propto \mathrm{P}(X \mid \theta)\,\mathrm{P}(\theta)$, where $\mathrm{P}(X \mid \theta)$ is the likelihood and $\mathrm{P}(\theta)$ is the prior. This expression is a parametric function of θ and indicates that our state of knowledge in θ given our observations X is proportional to the probability of those observations given the parameters, $\mathrm{P}(X \mid \theta)$, and to our prior state of knowledge in those parameters, $\mathrm{P}(\theta)$. Practically, the likelihood takes the form of a noise model—that is, we suppose the observations are distributed about the model predictions with some noise. We assume here a Gaussian likelihood joint over the two kinds of data,

$$\begin{aligned}
&\mathrm{P}\left(X \mid \theta, \left\{\sigma_{N_s}^{(k)}\right\}, \left\{\sigma_I^{(k)}\right\}\right) \\
&= \prod_{k=1}^{N_d} \frac{1}{\sigma_{N_s}^{(k)}\sqrt{2\pi}} \exp\left[-\frac{\left(N_s(V^{(k)}, \theta) - N_s^{(k)}\right)^2}{2\left(\sigma_{N_s}^{(k)}\right)^2}\right] \\
&\quad \times \frac{1}{\sigma_I^{(k)}\sqrt{2\pi}} \exp\left[-\frac{\left(I(V^{(k)}, \theta) - I^{(k)}\right)^2}{2\left(\sigma_I^{(k)}\right)^2}\right].
\end{aligned} \tag{19}$$

Here, $N_s(V^{(k)}, \theta)$ and $I(V^{(k)}, \theta)$ denote, respectively, the model-predicted number of sites and the model-predicted current, which are functions of voltage and the parameters θ. Similarly, $\sigma_{N_s}^{(k)}$ and $\sigma_I^{(k)}$ are the magnitudes of noise in the kth number of sites datum and the kth current datum—the standard deviations of the Gaussian distribution in Eq. (19). We have neglected error in the voltage data as they are known comparatively precisely (within 2 V on the scale of 1–2 kV) and will contribute little to the overall uncertainty.

We have also assumed here that the error in each datum is independent and have noted explicitly that this expression is conditioned on knowledge of the σ's. While in principle this noise can be determined from experimentally reported uncertainty, the error in counting individual sites is difficult to quantify, and it is challenging to assess uncertainty in the current at the small levels inherent to individual emitters. In lieu of leveraging the reported uncertainties from Ref. 16, then, we adopt a hierarchical Bayesian inference scheme. As such, we treat the noise terms as additional model parameters—denoted "hyperparameters"—and learn them alongside the data. To this end, we consider the simple noise models,

$$\sigma_{N_s}^{(k)} = \sqrt{a_{N_s}}, \tag{20}$$

$$\sigma_{I}^{(k)} = \sqrt{a_{I}}. \tag{21}$$

That is, for each kind of data (number of sites or current), the magnitude of noise in those data is a constant. We use a to denote the variance of the noise. For the additional datum, $x^{(0)}$, which we introduced to reflect the fact that no emission sites occur below 1100 V, we take $\sigma_{N_s}^{(0)} = 10^{-4} \times \sqrt{a_{N_s}}$ and $\sigma_{I}^{(0)} = 10^{-4} \times \sqrt{a_{I}}$. This reflects heuristically that we are confident that there is no emission at this voltage.

These variances constitute the hyperparameters $\varphi = (a_{N_s}, a_I)$, and so the hyperparametric posterior is

$$\mathrm{P}(\theta, \varphi \mid X) \propto \mathrm{P}(X \mid \theta, \varphi)\, \mathrm{P}(\theta)\, \mathrm{P}(\varphi), \tag{22}$$

where we have assumed the prior over φ is independent of that over θ. In this way, the likelihood of Eq. (19) is a parametric function of φ as well, $\mathrm{P}\left(X \mid \theta, \left\{\sigma_{N_s}^{(k)}\right\}, \left\{\sigma_{I}^{(k)}\right\}\right) = \mathrm{P}(X \mid \theta, \varphi)$.

Finally, we must assign a prior to the model parameters, θ, and hyperparameters, φ. Having not made any prior inference over these models, we choose uniform distributions as shown in Table III, which do not significantly constrain the parameter space. The bounds on ζ_0 and m reflect that they could in principle take any value, while those on ζ_1, p_2, a_{N_s}, and a_I reflect that they can take any non-negative value. The surface wetting coefficient, ψ, is bounded on [0, 1] by definition (see Sec. II B).

TABLE III. Prior distributions for current emission model parameters, surface wetting parameters, and noise hyperparameters.

Parameter	Prior distribution
ζ_0	$\mathscr{U}(-\infty, \infty)$
ζ_1	$\mathscr{U}[0, \infty)$
ψ	$\mathscr{U}[0, 1]$
p_2	$\mathscr{U}[0, \infty)$ m
m	$\mathscr{U}(-\infty, \infty)$
a_{N_s}	$\mathscr{U}[0, \infty)$
a_I	$\mathscr{U}[0, \infty)\ \mu\mathrm{A}^2$

IV. RESULTS

In this section, we present the results of fitting our model to the training dataset. First, we give model predictions and compare these with the observed data to assess model goodness-of-fit. Second, we show distributions over the model parameters to highlight their best-fit values and the correlations between them.

A. Model predictions

To generate model predictions subject to both model and experimental uncertainty, we adopted an algorithmic approach based on Bayesian inference. Consistent with Eq. (19) and the priors, Table III, we drew 10^6 samples from the posterior distribution $\mathrm{P}(\theta, \varphi \mid X)$ using a Markov chain Monte Carlo sampling algorithm (cf. Ref. 40). We translate these sampled parameters into model predictions at a given emitter voltage, V, by taking the model parameters from each sample, $\theta^{(i)}$, and evaluating the model [Eqs. (5) and (14)] at this voltage for these parameters. We use the predicted number of sites, N_s, and emitter current, I, from the model as the means of normal distributions with variance given by the inferred noise, which is given by the hyperparameters, $\varphi^{(i)}$. These distributions represent the impact of experimental uncertainty and allow a direct comparison of the model predictions to real data. We thus sample from these distributions once to yield the model prediction for this value of the parameters. Repeating this process for many samples, we compute the median and 90% credible interval at this voltage. We subsequently repeat this for each voltage investigated.

Figure 5 shows the results for the predicted current and number of emission sites as a function of discharge voltage. As one can see, the median model predictions (solid lines) closely track the experimental data (blue circles), and a majority of the experimental data are enveloped by a 90% credible interval (shaded region between dashed lines).

In addition to capturing general trends, the trained model also duplicates key features of the two kinds of experimental observations. For the predicted number of active sites [Fig. 5(a)], the model reproduces the experimental observation that there is only of order a single emission site near emission onset, but that this increases to 9 sites at 2000 V. Within the noise of the data, the model successfully discerns a weak inflection in the number of sites across the domain. For the emitter current [Fig. 5(b)], the model is able to capture that while sites are observable below 1300 V, they carry little current, less than 110 nA. The model then predicts the emission current is strongly inflected until about 1500 V, where it saturates toward being linear with voltage. We remark here that the ability to capture these trends would not be possible in a model where the variance in emission site size is not included. We return to this point in the discussion (Sec. V).

B. Parameter distributions

We next consider the distributions over these model parameters. To this end, we provide in Table IV several statistical measures of the distribution. First, we give the *maximum a posteriori* (MAP) sample, the sample drawn with the highest posterior probability. This is the mode of the posterior distribution and represents the

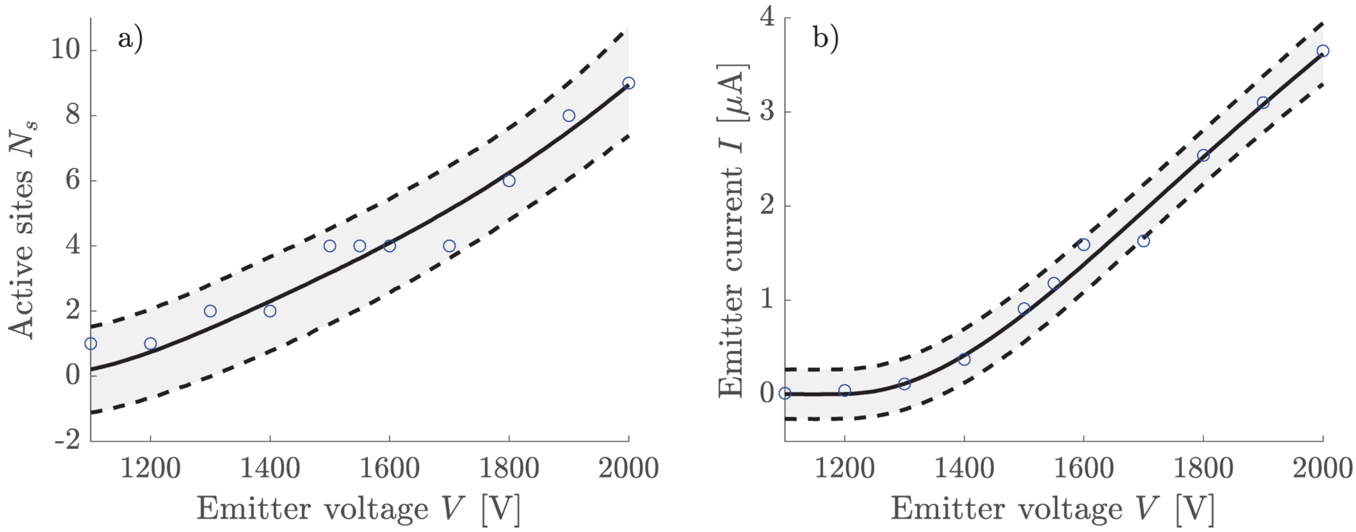

FIG. 5. Posterior predictions (a) for the number of active sites, N_s, and (b) for the emitter current, I; the solid black line is the median prediction, the dashed black lines and shaded region are a 90% credible interval centered at the median, and the training data[16] are plotted as blue circles.

single best estimate to the parameters (i.e., a least squares fit to the data). Alongside this single sample, we display the median, mean, and standard deviation for each parameter and hyperparameter taken over all 10^6 samples. The median and mean serve as alternative point estimates to the parameters, and the standard deviation acts as a simplified measure of uncertainty in the parameters. If the standard deviation is small on the scale of the parameters (e.g., for ψ), this suggests this model parameter is well determined from the data and vice versa for large standard deviation (e.g., for m).

The current emission parameters ζ_0 and ζ_1 determine how sensitive the ion current is to the applied field. We previously trained a similar parameterization for current emission on experimental data for the AFET-2 thruster, which has comparable emitter geometry.[40] We note that the $\zeta_1 \approx 0.04$ found here agrees well with the value found in Ref. 40 for an equivalent parameter (≈ 0.02). We also note that, interestingly, ζ_0 has taken a negative value, indicating [see Eq. (13)] that Taylor cones form at one voltage but are predicted not to emit appreciable current until a modestly higher voltage.

The parameters ψ, p_2, and m describe the meniscus population that forms on the surface of the emitter. The value $m = 1.31$ confirms our qualitative comparison to other filming phenomena for which the number density is inversely proportional to feature size,[31] but the large standard deviation means model predictions are insensitive to this parameter given the experimental data. Our inference on ψ indicates that about 11% of the emitter surface is wetted. This is lower than the volumetric wetting of the substrate, which for the P5 frit used here should be about 48%.[38] Physically, this may indicate that the surface is approximately four times less wet than the substrate could in principle support. Similarly, our values of p_2 indicate that menisci reach sizes as large as 7 μm in diameter. This is several times larger than the maximum pore size in the frit (1.6 μm) and suggests that the propellant can pool outside of pores. While others have hypothesized the existence of this pooling previously,[16,29,30,40,41] our work indicates that this degree of pooling is necessary to explain the observed trends in onset and current.

To better interrogate relationships between parameters, we show a corner plot of posterior samples in Fig. 6, where we have marginalized over the uncertain hyperparameters, $P(\theta \mid X) = \int P(\theta, \varphi \mid X)\, d\varphi$. The structure of this corner plot resembles that of a covariance matrix, with the diagonal entries representing 1d marginal distributions for each parameter and the off-

TABLE IV. Maximum *a posteriori* parameter (MAP) sample alongside the median, mean, and standard deviation over all 10^6 samples of each parameter.

Parameter	MAP sample	Median	Mean	Standard deviation
ζ_0	-4.50×10^{-3}	-4.19×10^{-3}	-5.07×10^{-3}	5.69×10^{-3}
ζ_1	4.14×10^{-2}	4.01×10^{-2}	4.50×10^{-2}	2.84×10^{-2}
ψ	0.115	0.113	0.114	0.009
p_2	7.11 μm	6.92 μm	6.82 μm	0.60 μm
m	1.31	1.33	1.30	0.82
a_{N_s}	0.271	0.510	0.685	0.649
a_I	$1.31 \times 10^{-2}\, \mu A^2$	$2.17 \times 10^{-2}\, \mu A^2$	$2.68 \times 10^{-2}\, \mu A^2$	$2.02 \times 10^{-2}\, \mu A^2$

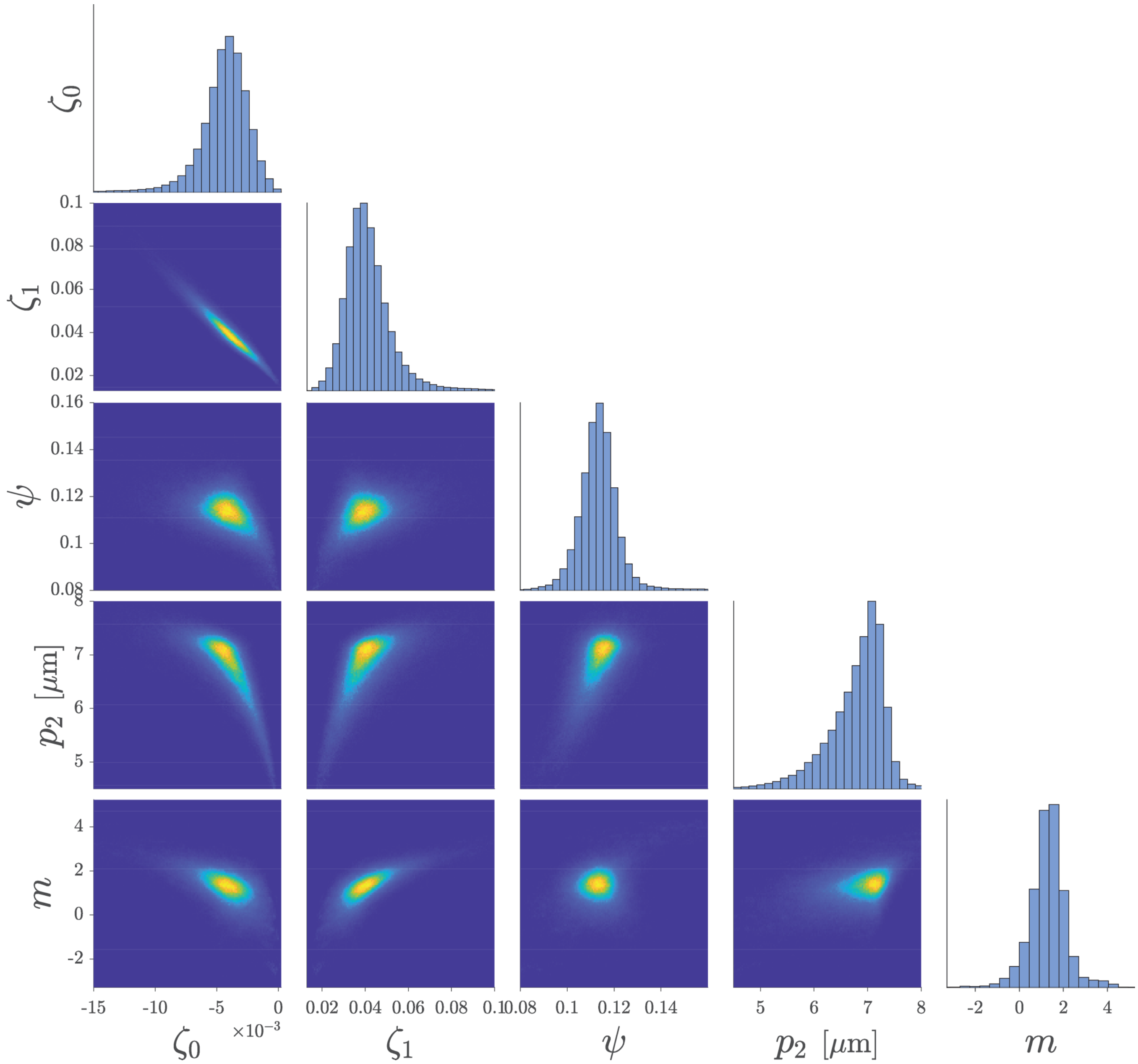

FIG. 6. Samples of posterior $\mathrm{P}(\theta \mid X)$ for $\theta = (\zeta_0, \zeta_1, \psi, p_2, m)$; the plot is constructed as a covariance matrix: the diagonal entries are histograms of each parameter, and the off-diagonal entries are 2d histograms of the associated two-parameter subspace.

diagonal entries representing 2d marginal distributions for each pair of parameters. For example, the top left entry corresponds to $\mathrm{P}(\zeta_0 \mid X) = \int \mathrm{P}(\theta \mid X)\,\mathrm{d}\zeta_1\,\mathrm{d}\psi\,\mathrm{d}p_2\,\mathrm{d}m$, and the bottom left entry is $\mathrm{P}(\zeta_0, m \mid X) = \int \mathrm{P}(\theta \mid X)\,\mathrm{d}\zeta_1\,\mathrm{d}\psi\,\mathrm{d}p_2$.

The figure demonstrates that the parameters are largely uncorrelated, as evidenced by the several broad distributions in the 2d marginals. This independence of the model parameters suggests the physical processes we are modeling are separable from each other. A key exception exists between ζ_0 and ζ_1, which Fig. 6 shows are strongly anticorrelated. This correlation is likely a consequence of the linearization in Eq. (12), which ignores the complex behavior near emission onset. We examine this interplay further in the discussion (Sec. V). We note here as well that while there are other correlations evident in the figure (most notably between p_2, ζ_0, and ζ_1), these are largely limited to low-probability tails, which represent unlikely parameter values. In summary, the key funding from this analysis is that this model is able to capture the key behavior of the emission sites with largely independent model parameters.

V. DISCUSSION

We discuss in detail in this section the key trends of the results presented in Sec. IV. First, we examine the emission behavior, highlighting the effects of the meniscus size distribution and the position-dependent electric field. We next contrast the properties of the inferred menisci population with the pore size distribution in the substrate and explore the extensibility of our model. Finally, we discuss the value of our model within the inherently probabilistic problem of designing arrays of many electrospray emitters.

A. Trends in the number of emission sites and total current with voltage

As we showed through our results (Sec. IV), our model successfully captures key elements of the nonlinear emission behavior with voltage (see Fig. 5). These macroscopic predictions arise from two key effects. First, as a result of the position-dependent electric field, $E(s)$ (see Fig. 3), the area of the emitter that participates in emission increases with voltage. Second, convolved with $f(p)$, the number of sites and current per unit area over this domain increase with voltage. To illustrate the interplay between these two effects, we evaluated the model for the MAP value of the parameters (see Table IV) at several voltages over the domain. Rather than performing the exterior integrals over s as in Eqs. (5) and (14), however, we left the model predictions in terms of the site density per unit area, $\bar{1}_O\, n_p$, and current density per unit area, $\bar{i}\, n_p$, which vary as a function of s. We plot these densities as functions of s for six different voltages in Figs. 7(a) and 7(b),

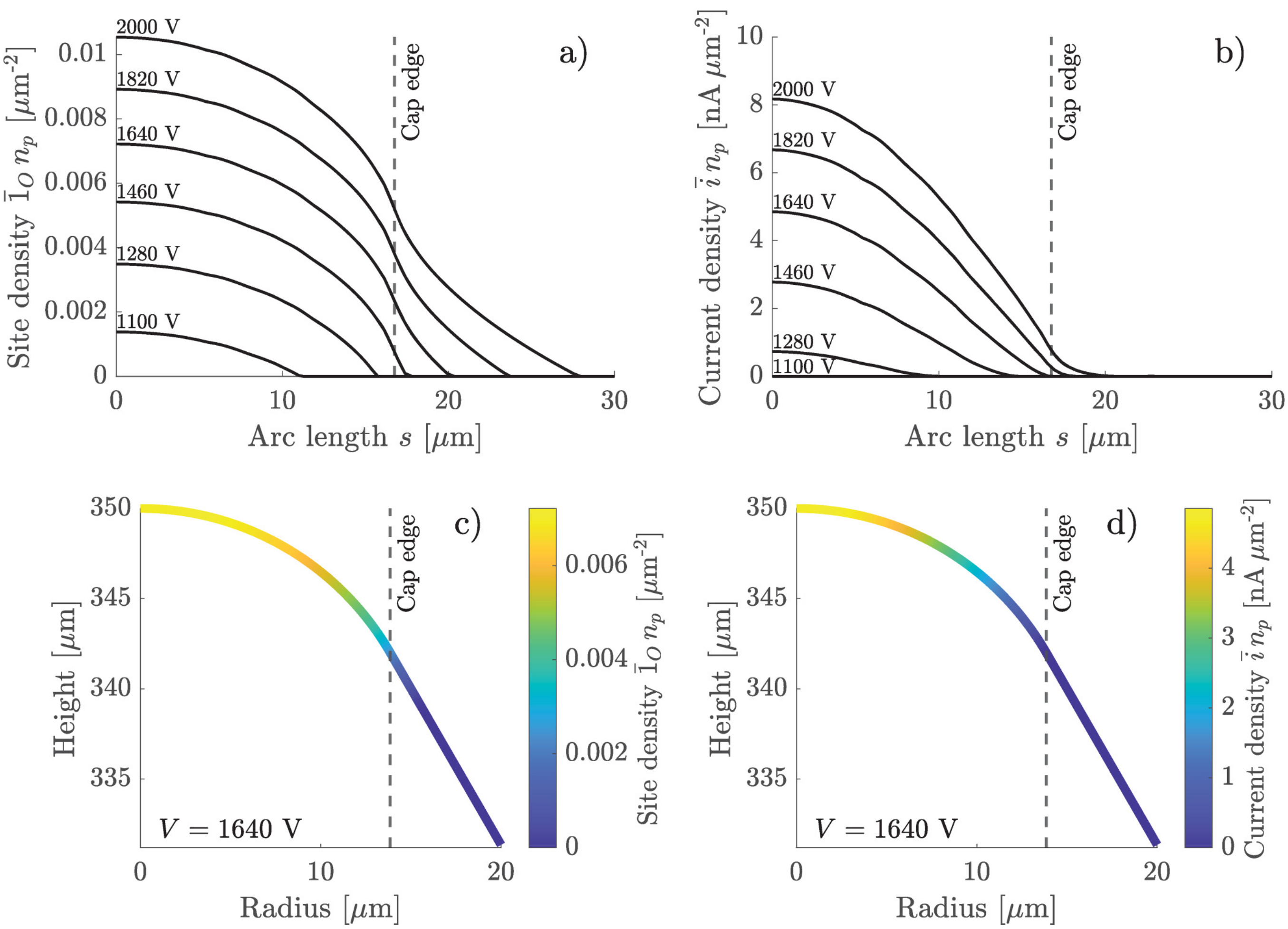

FIG. 7. Position-dependent site density, $\bar{1}_O\, n_p$, and current density, $\bar{i}\, n_p$, near the emitter apex for the MAP estimate to the parameters (see Table IV); site (a) and current (b) density as a function of arc length, s, along the emitter, for six different voltages; site (c) and current (d) density as a heatmap on the emitter cross section for $V = 1640$ V; the edge of the emitter cap is shown for reference.

respectively. In Figs. 7(c) and 7(d), we also plot these densities for a single voltage ($V = 1640\,\text{V}$) but as heatmaps resolved on the 2d cross section of the emitter near its apex.

1. Number of sites

The trends in number of emission sites with voltage exhibited in Fig. 5 can be explained from the onset criterion [Eq. (8)]. At lower voltages, the electric field is only strong enough to satisfy the onset criterion (for any meniscus size) at the very apex of the emitter. As voltage increases, however, the field toward the edges of the emitter tip grows sufficiently strong to satisfy the onset criterion as well, and sites begin to appear progressively farther away from the central axis of the emitter. One can observe this behavior as an increase in the maximum s for which the site density is nonzero in Fig. 7(a). This interpretation is consistent with spatially resolved measurements of the emission current for the dataset we have considered here (cf. Ref. 16). Indeed, that work showed that the first beamlets develop close to the axis of the emitter, but later beamlets occurred at wider angles. More broadly, this behavior—that secondary emission sites forming at higher voltages produce beams at angles far from the initial site—has repeatedly been observed.[14,15,18,19]

Additionally, once the onset criterion is first satisfied for at least one possible meniscus size at a given location, the site density is predicted to increase with voltage, as is evident in Fig. 7(a). Physically, this arises from the fact that for lower voltages, only the largest menisci—those with the smallest capillary pressure to resist the applied field—are active. As the field increases, the onset criterion is satisfied for progressively smaller menisci, increasing the proportion of active sites, $\bar{1}_O$ [see Eq. (10) and the Appendix]. The product of these two effects—increasing effective emission area and increasing density of emission sites with voltage—explains the nonlinear rise in the number of sites.

2. Total current

For the total emitted current, similar trends are evident in Fig. 7(b) but are explained by a more subtle interplay of mechanisms. While Eq. (14) predicts the current to increase with voltage due to the increased number of emission sites, the hydraulic impedance to each individual site also increases as more sites are created [see Eq. (16)]. This is because the total hydraulic impedance of the emitter is constant. The increased impedance to flow reduces the current per site for a given voltage and causes the site density at a given point [see Fig. 7(b)] to grow more slowly than linearly with voltage. Decreasing current per site was observed experimentally at higher discharge voltages in Ref. 16.

This increase in hydraulic impedance serves to exactly counterbalance the increase in total current with a larger number of sites. At sufficiently high voltages, the amount of current emitted is thus independent of the number of emission sites. The total current consequently scales only as the driving pressure—the electric pressure minus the capillary pressure—which is predicted to be linear with voltage per Eq. (13). This balance produces the linear growth of current with voltage evident in the training data.

A notable implication of this finding is that the I–V trace for a single emitter at voltages beyond onset will be independent of the number of emission sites that form. In practice, this could suggest that multi-site emission is commonplace in porous emitters and cannot be fully de-convolved solely through inspection of the total current with applied voltage. We qualify this observation with the fact that these conclusions apply to effective averages over the properties of the emitter, such that there may be perturbations from this bulk trend. We return to this point in Sec. V D.

The linear behavior with voltage breaks down as we approach the onset threshold at 1100 V. Instead, we observe a smooth, nonlinear rise in current with voltage, consistent with the training data (see Fig. 5). This trend appears as a result of the distribution over meniscus size, $f(p)$. Equation (13) predicts that the current produced by a site is inversely proportional to its size, such that smaller menisci produce larger currents for the same applied field. This dependency arises because the Taylor cones formed from smaller menisci more strongly concentrate the electric field at their apexes, providing enhanced extraction.[35] As such, unlike in the high voltage case where the current per site decreases due to the rising hydraulic impedance at each site, the average current per site, $\bar{i}(E(s))$ increases for low voltages. This leads to the initial nonlinear behavior exhibited in Figs. 5 and 7(b).

B. Disparity in meniscus and pore size

As discussed in Sec. II B, one of the key findings from the model inference is that the surface wetting parameters ψ and p_2 are not consistent with what we would expect given the physical properties of the substrate. For the P5 frit from which the emitter was fabricated, the pore size is quoted as distributed between 1 and $1.6\,\mu$m, and the substrate is estimated to be 48% void.[38] If the menisci on the surface were tied exactly to these "pores," we would expect $p_2 = 1.6\,\mu$m and $\psi = 0.48$, but as Table IV illustrates, we found $p_2 = 7.0\,\mu$m and $\psi = 0.11$.

The relatively large value of p_2 arises physically from the onset criterion [Eq. (8)]. Given the propellant properties of Table II and the field amplification of the emitter of Fig. 3, menisci of size $p = 1.6\,\mu$m are not predicted to activate below 1900 V. The experimental observation of an emission site at 1100 V indicates the presence of menisci substantially larger than this pore size, with correspondingly lower capillary pressure to resist onset. That p_2 is larger than the maximum pore size is consistent with the notion that propellant pools outside of pores. As discussed in Sec. IV B, previous authors have suggested this type of pooling is necessary to explain emission behavior.[16,30]

The value of the surface wetting coefficient we inferred here, $\psi = 0.11$, indicates physically that only 11% of the emitter surface is wetted by propellant. This is a factor of four lower than the substrate potentially could support, given that it is 48% void by volume. This result taken together with our inference over p_2 suggests a physical picture for the emitter as a surface consisting of a sparse population of large fluid oases. Previous authors have posited mechanisms to explain why this type of configuration may occur, ranging from fluid recession into the substrate with increased electric traction[16,41] to the formation of periodic pressure structures on the emitter.[27] Additional experiments are ultimately warranted to verify these conclusions and interrogate these potential mechanisms.

With that said, the inability to fully predicate the meniscus distribution on the bulk fluidics of the substrate justifies our abstraction of the surface wetting through $f(p)$ and ψ. In the absence of a more thorough characterization of the surface pores (e.g., by optical[42] or radiographic[43] techniques) and without a model able to predict the resulting meniscus formation, parameterizing this distribution and regressing from data is expedient. However, by fitting to the data in this way, we may limit the applicability of these values, a point we discuss more broadly in Sec. V C.

C. Extensibility of model

While our model was successful in reproducing trends in an experimental dataset, the question remains as to how extensible the regressed model parameters are to other systems. With respect to the ionic emission model, Coffman *et al.* argue that the dimensionless parameters ζ_0 and ζ_1 should be universal properties of ionic sprays.[3] Our results support that this is the case for ζ_1, the characteristic slope of ionic emission. Indeed, in previous work where we inferred this parameter for a thruster with different geometry and operating on a different propellant, we found a value $\zeta_1 \approx 0.02$.[40] This is within the marginal uncertainty of the value of $\zeta_1 = 0.04$ we inferred here (Fig. 5). We draw this comparison with the qualification that Ref. 40 used a modestly different parameterization of Eq. (13). However, for higher operating voltages where the applied electric field is large on the scale of the onset field and reservoir pressure, $E(s) \gg E_0$, these parameterizations should converge.

For ζ_0, the offset in the ionic emission scaling law, this difference in parameterization means we do not have a previous value for direct comparison. We can make a more general comment about its universality, however, in light of our observation that ζ_0 has a negative value for our present work. Negative ζ_0 implies that Taylor cones form at one voltage but do not begin shedding appreciable charge until a higher voltage. This produces the macroscopic lag between when the first emission site is observed ($\sim$1100 V) and when current begins to grow ($\sim$1300 V) in Fig. 5. This phenomenon has been observed in similar emitters,[18,44] but it is also common instead to see a jump discontinuity in current with onset of the first emission site,[11,15,18,19] which would be consistent with a positive value of ζ_0. This disagreement suggests that ζ_0 is not universal, a result of the richer physics[3,34,35] ignored in performing the linearization of Eq. (12).

With respect to the surface wetting parameters (ψ, p_2, and m), we anticipate that our results are more limited because we captured the meniscus population by a phenomenological size distribution, $f(p)$. In so doing, we abstracted away the microscopic structure and wetting properties of the substrate. For emitters of different chemical composition, pore size and shape, or methods of fabrication, these results likely do not map fully. For example, while our inference showed a surface wetting lower than the volumetric porosity of the substrate, Wright[45] observed the opposite trend in a porous tungsten source operating on the same propellant. When applying the model to emitters constructed from similar substrates using like manufacturing methods, however, these parameters may not change appreciably. This invites the possibility that after training the model, we could consider the parameters as known quantities of the emitter material, much as we treat the substrate's permeability or the fluid properties of the propellant.

Last, provided we have values for the physics-based model parameters, e.g., the properties of ionic emission and surface wettability, our model formulation is readily extensible to alternative geometries. In the case of other porous conical emitters, this is captured through changes in the geometric parameters (e.g., R_c and h) and a recomputation of the corresponding field profile, $E(s)$. For other geometries, like porous wedge systems, the scaling arguments and formalism underlying the model are still valid. As such, the model can be extended to these geometries by adapting the surface area parameterization, dA, and the model for hydraulic impedance, R_h.

D. Implications for array modeling and optimization

The statistical methodologies explored in this work are well suited to the practical problem of designing arrays of many electrospray emitters. As discussed in Sec. I, while electrospray thrusters offer several potential advantages for in-space propulsion,[4] these advantages come with the cost that single emitters produce very little thrust, less than 1 μN. It is therefore necessary to aggregate many together to achieve sufficient thrust, with systems of many hundred emitters having been demonstrated.[9,15,46,47]

There are several challenges with modeling this type of array configuration predictively. Electrospray emitters are multi-scale devices, from the atomic scale of ionic emission[3,48] to the macroscopic scale of plume interactions.[49,50] In principle, resolving all these phenomena at high fidelity requires a detailed and computationally intensive simulation.[48,51] Resolving each emitter in an array of hundreds or thousands of emitters at such fidelity would thus be impractical.

A possible strategy to overcome this limitation is to take a high fidelity prediction for a single emitter and scale it by the number of emitters in the array. Such a strategy would be ill-posed, however, because it does not account for variability in emitter behavior across the array. Sources of variability include inhomogeneous fluidic boundary conditions,[14] manufacturing tolerances in emitter geometry and alignment,[40,52] and the stochastic nature of the underlying substrate (i.e., that the particular arrangement of menisci on the surface of each emitter is variable). This type of emitter-to-emitter variance is problematic, as it greatly increases the probability of system failure[26] and can lead to unwanted artifacts such as vectored thrust.[53] As such, accounting for emitter-to-emitter differences in modeling and simulations is necessary to accurately predict the performance of an array.

The need to account for emitter nonuniformity motivates a modeling strategy that can capture multi-emitter behavior—subject to variability—but in a computationally inexpensive way. Our emitter model is an attractive tool for this purpose, capable of O (10^6) evaluations in only an hour's time on a single contemporary CPU core. This speed comes at the sacrifice of fidelity, however. Our models have parameters that must be calibrated from data, and the uncertainty in these parameters contributes additional uncertainty to our predictions.

To capture this model uncertainty, we have adopted a Bayesian statistical formalism where we represent the model as probabilistic predictions with credible intervals (see Fig. 5). These communicate our uncertainty in how any one emitter will behave. Such probabilistic results lend themselves to a physically intuitive interpretation when applied to modeling an array: if the median prediction for a given voltage is 2.5 sites, for example, and we were to manufacture an array with many emitters, the average number of sites per emitter at that voltage would be 2.5.

In this work, we did not consider uncertainty in emitter geometry, as we focused on a single emitter with known dimensions. As a result, our predictions account for uncertainty in the model parameters, uncertainty in the data, and emitter variability stemming from the distribution of menisci on the surface. The formermost is captured by sampling over the posterior distribution over model parameters, while the latter two are captured through our hyperparametric treatment of the noise. Our formalism is readily extended to array geometries by representing variations in dimensions as probabilistically distributed due to manufacturing tolerance.[40,52]

Altogether then, these methodologies serve as valuable new tools in the design of electrospray arrays, particularly in performing model-based design under uncertainty.[54] The computational economy of the model permits rapid evaluations suited to a search through design space, and the rigorous statistical treatment supports making predictions with confidence. Moreover, the formalism provides a framework in which model confidence can be increased with targeted experiments. As more arrays are built and tested, the confidence in the model improves.

VI. CONCLUSION

In this work, we motivated a physics-based model to represent the number of emission sites and total current of a porous conical electrospray emitter. We focused on the role of two processes in particular: (1) the menisci that form on the emitter surface have variable size and activate at different voltages, and (2) the variation in electric field strength across the emitter surface leads to a wider active area on the emitter with increasing voltage. To capture these effects, we have developed a reduced fidelity model that allows for a phenomenological distribution of meniscus size and a variable electric field strength with position. We combined these models with scaling laws for the onset of Taylor cones and ionic current emission and then integrated these over both the emitter geometry and the distribution in meniscus sizes. This yielded probabilistic predictions of the expected number of emission sites and current.

The adoption of reduced fidelity scaling laws and phenomenological descriptions for the meniscus distribution required the introduction of free model parameters. To determine these, we applied Bayesian inference to regress our model against data previously measured for a porous conical electrospray emitter. This provided probability distributions for the model parameters as well as distributions for the overall model predictions. From these results, we in turn showed that a key parameter governing ionic emission—the non-dimensional slope of current with voltage—agrees well with previous studies on ionic emission. We also found that the predicted meniscus size can exceed the average pore size of the emitter, while the overall surface is less than 11% fully wetted. This suggests a physical picture in which the emitter is characterized by a series of large pools of propellant spaced sparsely on the emitter.

We demonstrated through our model predictions that our model captured the experimental data within error, with a majority of the experimental data falling within a 90% credible interval. Key trends we reproduced included positively inflected growth in the number of emission sites with voltage and the transition to approximately linear growth in current after a nonlinear region near onset. We, in turn, leveraged our model to offer physical explanations for these trends as trades among the size of emitters activated, the change in hydraulic impedance per emission site, and the total number of activated sites.

In addition to explaining the existing training dataset, we also discussed the extensibility and possible applications of this work. In particular, we noted that the methodologies explored here are powerful tools for continued electrospray design. This stems largely from the fact that our model formulation is particularly amenable to predicting performance of arrays of electrospray emitters (e.g., as part of model-based design optimization). Such problems are inherently probabilistic, as they must account for emitter-to-emitter variance in performance and so require many model evaluations. The present model also has the advantage that it is computationally inexpensive, lending itself to a statistical framework that makes emitter variability readily interrogable. In summary, we have presented in this work a new framework for accounting for multi-site emission in porous electrosprays with uncertainty at scale. This contribution ultimately represents a necessary step toward developing the insights and modeling and simulation tools necessary for advancing this technology for in-space propulsion applications.

SUPPLEMENTARY MATERIAL

The data used in and generated by this study are included in the supplementary material. We also provide all the computer code used to process and generate these data, including an implementation of the multi-site emission model in Python.

ACKNOWLEDGMENTS

This work was supported by an Early Stage Innovations grant from NASA's Space Technology Research Grants Program (80NSSC19K0219) and by a NASA Space Technology Graduate Research Opportunity (80NSSC21K1247). The authors would like to thank Rainer Dressler, Benjamin St. Peter, and John Yim for their early feedback on the model and Busek Co. Inc. for furnishing an image of their test article. The authors would also like to thank William Hurley for his assistance in setting up the COMSOL simulations.

AUTHOR DECLARATIONS

Conflict of Interest

The authors have no conflicts to disclose.

Author Contributions

C. B. Whittaker: Conceptualization (equal); Data curation (lead); Formal analysis (lead); Funding acquisition (equal); Investigation (lead); Methodology (lead); Software (lead); Validation (lead); Visualization (lead); Writing – original draft (lead); Writing – review & editing (equal). **B. A. Jorns:** Conceptualization (equal); Formal analysis (supporting); Funding acquisition (equal); Methodology (supporting); Project administration (lead); Resources (lead); Writing – original draft (supporting); Writing – review & editing (equal).

DATA AVAILABILITY

The data that support the findings of this study are available within the article and its supplementary material.

APPENDIX: ALGORITHMS FOR COMPUTING MOMENT LIMITS

Algorithm 1 gives how to compute the bounds in p space over which the moment $\bar{\imath}_O(E(s))$ [Eq. (10)] is taken, $p \in [p_{O,1}, p_{O,2}]$. Algorithm 2 gives the same for where the moment $\bar{\imath}(E(s))$ [Eq. (13)] is taken, $p \in [p_{I,1}, p_{I,2}]$. See also the model implementation in the supplementary material.

ALGORITHM 1. Computing $p_{O,1}$ and $p_{O,2}$.

Output: minimum meniscus size for onset $p_{O,1}$, maximum meniscus size for onset $p_{O,2}$

$a = -\frac{\beta_1 P_r}{4\gamma}$;

$b = -\sqrt{\frac{1}{2}\varepsilon_0 \frac{1}{4\gamma}} E(s)$;

$c = \beta_0$;

if $P_r = 0$ **then**

  $p_{O,1} = \frac{c^2}{b^2}$;

  $p_{O,2} = p_2$;

else if $P_r < 0$ **then**

  if $b^2 \leq 4ac$ **then** no onset $\forall p$

    $p_{O,1} = p_{O,2} = 1$;

  else

    $p_{O,1} = \left(\frac{-b-\sqrt{b^2-4ac}}{2a}\right)^2$;

    $p_{O,2} = \left(\frac{-b+\sqrt{b^2-4ac}}{2a}\right)^2$;

  end

else $P_r > 0$

  $p_{O,1} = \left(\frac{-b-\sqrt{b^2-4ac}}{2a}\right)^2$;

  $p_{O,2} = p_2$;

end

$p_{O,1} = \max(p_{O,1}, p_1)$;

$p_{O,2} = \min(p_{O,2}, p_2)$;

if $p_{O,1} > p_{O,2}$ **then** no onset on $[p_1, p_2]$

  $p_{O,1} = p_{O,2} = 1$;

end

ALGORITHM 2. Computing $p_{I,1}$ and $p_{I,2}$.

Input: minimum meniscus size for onset $p_{O,1}$, maximum meniscus size for onset $p_{O,2}$

Output: minimum meniscus size for current $p_{I,1}$, maximum meniscus size for current $p_{I,2}$

$a = \zeta_1 \beta_1 P_r$;

$b = \sqrt{\frac{4\gamma\varepsilon_0}{2}} E(s) \zeta_1$;

$c = 4\gamma(\zeta_0 - \zeta_1 \beta_0)$;

if $P_r < 0$ **then**

  if $b^2 \leq 4ac$ **then** no current $\forall p$

    $p_{I,1} = p_{I,2} = 1$;

  else

    $p_{I,1} = \left(\frac{-b-\sqrt{b^2-4ac}}{2a}\right)^2$;

    $p_{I,2} = \left(\frac{-b+\sqrt{b^2-4ac}}{2a}\right)^2$;

  end

else if $c > 0$ **then** current $\forall p \in [p_1, p_2]$

  $p_{I,1} = p_1$;

  $p_{I,2} = p_2$;

else if $P_r > 0$ **then**

  $p_{I,1} = \left(\frac{-b+\sqrt{b^2-4ac}}{2a}\right)^2$;

  $p_{I,2} = p_2$;

else $P_r = 0$

  $p_{I,1} = \frac{c^2}{b^2}$;

  $p_{I,2} = p_2$;

end

$p_{I,1} = \max(p_{I,1}, p_{O,1})$;

$p_{I,2} = \min(p_{I,2}, p_{O,2})$;

if $p_{I,1} > p_{I,2}$ **then** no current on $[p_1, p_2]$

  $p_{I,1} = p_{I,2} = 1$;

end

REFERENCES

[1]G. I. Taylor, Proc. R. Soc. London Ser. A: Math. Phys. Sci. **280**, 383–387 (1964).
[2]A. M. Gañán-Calvo, J. M. López-Herrera, M. A. Herrada, A. Ramos, and J. M. Montanero, J. Aerosol. Sci. **125**, 32–56 (2018).
[3]C. Coffman, M. Martinez-Sanchez, F. Higuera, and P. C. Lozano, Appl. Phys. Lett. **109**, 231602 (2016).
[4]P. C. Lozano, B. L. Wardle, P. Moloney, and S. Rawal, MRS Bull. **40**, 842–849 (2015).
[5]V. Hruby, M. G.-C. No, P. Falkos, and S. Shenoy, in *27th International Electric Propulsion Conference* (Electric Rocket Propulsion Society, 2001), p. 281.
[6]A. Cisquella-Serra, M. Galobardes-Esteban, and M. G.-C. No, ACS Appl. Mater. Interfaces **14**, 43527 (2022).
[7]P. Lozano and M. Martinez-Sanchez, J. Colloid Interfacial Sci. **282**, 415 (2005).
[8]R. S. Legge and P. C. Lozano, J. Propul. Power **27**, 485 (2011).
[9]M. R. Natisin, H. L. Zamora, W. A. McGehee, N. I. Arnold, Z. A. Holley, M. R. Holmes, and D. Eckhardt, J. Micromech. Microeng. **30**, 115021 (2020).
[10]C. Coffman, L. Perna, H. Li, and P. C. Lozano, in *49th AIAA/ASME/SAE/ASEE Joint Propulsion Conference* (American Institute of Aeronautics and Astronautics, 2013), p. 4035.
[11]C. Perez-Martinez and P. Lozano, Appl. Phys. Lett. **107**, 043501 (2015).
[12]O. Jia-Richards, J. Appl. Phys. **132**, 074501 (2022).
[13]D. G. Courtney, "Ionic liquid ion source emitter arrays fabricated on bulk porous substrates for spacecraft propulsion," Ph.D. thesis (Massachusetts Institute of Technology, 2011).
[14]C. Guerra-Garcia, D. Krejci, and P. Lozano, J. Appl. Phys. D **49**, 115503 (2016).
[15]D. Krejci, F. Mier-Hicks, R. Thomas, T. Haag, and P. Lozano, J. Spacecr. Rockets **54**, 447 (2017).
[16]R. A. Dressler, B. St. Peter, Y.-H. Chiu, and T. Fedkiw, J. Propul. Power **38**, 809 (2022).
[17]M. R. Shcroeder, A. R. Bruno, and P. C. Lozano, in *AIAA SciTech 2022 Forum* (American Institute of Aeronautics and Astronautics, 2022), p. 0037.
[18]W. McGehee, N. Arnold, M. Natisin, Z. Holley, and D. Eckhardt, in *37th International Electric Propulsion Conference* (Electric Rocket Propulsion Society, 2022), p. 600.
[19]M. R. Shcroeder, X. Gallud, A. R. Bruno, O. Jia-Richards, and P. C. Lozano, in *AIAA SciTech 2023 Forum* (American Institute of Aeronautics and Astronautics, 2023), p. 1408.
[20]D. G. Courtney and H. Shea, Appl. Phys. Lett. **107**, 103504 (2015).
[21]D. G. Courtney, N. Alvarez, and N. R. Demmons, in *2018 Joint Propulsion Conference* (American Institute of Aeronautics and Astronautics, 2018), p. 4634.
[22]T. P. Fedkiw, Z. D. Wood, and N. Demmons, in *AIAA Propulsion and Energy 2021 Forum* (American Institute of Aeronautics and Astronautics, 2021), p. 3389.
[23]P. L. Wright, N. M. Uchizono, A. L. Collins, and R. E. Wirz, in *37th International Electric Propulsion Conference* (Electric Rocket Propulsion Society, 2022), p. 232.
[24]J. Ziemer, C. Marrese-Reading, C. Dunn, A. Romero-Wolf, C. Cutler, S. Javidnia, T. Le, I. Li, G. Franklin, P. Barela, O. Hsu, P. Maghami, J. O'Donnell, J. Slutsky, J. I. Thorpe, N. Demmons, and V. Hruby, in *35th International Electric Propulsion Conference* (Electric Rocket Propulsion Society, 2017), p. 578.
[25]N. A. Brikner, "On the identification and mitigation of life-limiting mechanisms of ionic liquid ion sources envisaged for propulsion of microspacecraft," Ph.D. thesis (Massachusetts Institute of Technology, 2015).
[26]B. A. Jorns, A. Gorodetsky, I. Lasky, A. Kimber, and P. Dahl, in *36th International Electric Propulsion Conference* (Electric Rocket Propulsion Society, 2019), p. 317.
[27]P. L. Wright and R. E. Wirz, Phys. Fluids **33**, 012003 (2021).
[28]F. A. L. Dullien, *Porous Media: Fluid Transport and Pore Structure*, 2nd ed. (Academic Press, Inc., 1992).
[29]B. St. Peter, R. A. Dressler, Y.-H. Chiu, and T. Fedkiw, Aerospace **7**, 91 (2020).
[30]X. Gallud-Cidoncha, B. O. Kristinsson, and P. C. Lozano, in *36th International Electric Propulsion Conference* (Electric Rocket Propulsion Society, 2019), p. 610.
[31]H. Cha, H. Vahabi, A. Wu, S. Chavan, M.-K. Kim, S. Sett, S. A. Bosch, W. Wang, A. K. Kota, and N. Miljkovic, Sci. Adv. **6**, eaax0746 (2020).
[32]M. Martinez-Sanchez, "Lecture 23-25: Colloidal Engines (Web, 2004), Lecture notes.
[33]F. J. Higuera, Phys. Rev. E **77**, 026308 (2008).
[34]C. S. Coffman, M. Martínez-Sánchez, and P. C. Lozano, Phys. Rev. E **99**, 063108 (2019).
[35]X. Gallud and P. C. Lozano, J. Fluid Mech. **933**, A43 (2022).
[36]S. Castro and J. F. de la Mora, J. Appl. Phys. **105**, 034903 (2009).
[37]C. S. Perez-Martinez and P. C. Lozano, J. Vac. Sci. Technol. B **30**, 06F601 (2012).
[38]ROBU Glasfilter-Geräte GmbH, "Vitrapor®sinterfilter pore properties," see https://www.robuglas.com/fileadmin/dateien/Bilder/Service/Downloads/Te%chnische_Daten_im_Detail_eng/poreproperties_vitrapor_e.pdf (2022) (last accessed June 10, 2022).
[39]SSI, Inc., "Espet web app," see http://espet.spectral.com/ (2022) (last accessed June 10, 2022).
[40]C. B. Whittaker, A. A. Gorodetsky, and B. A. Jorns, in *AIAA SciTech 2022 Forum* (American Institute of Aeronautics and Astronautics, 2022), p. 0041.
[41]P. L. Wright and R. E. Wirz, in *AIAA Propulsion and Energy 2021 Forum* (American Institute of Aeronautics and Astronautics, 2021), p. 3437.
[42]J. Rojas-Herrera, I. Jivanescu, D. Freeman, D. Krejci, C. Fucetola, and P. Lozano, J. Nanomech. Micromech. **7**, 04017006 (2017).
[43]S. Chamieh, E. Petro, and S. Sobhani, in *AIAA SciTech 2023 Forum* (American Institute of Aeronautics and Astronautics, 2023), p. 0261.
[44]C. Ma, T. Bull, and C. N. Ryan, J. Propul. Power **37**, 816 (2021).
[45]P. L. Wright, "Porous electrospray fluid mechanics," Ph.D. thesis (University of California, Los Angeles, 2022).
[46]L. Velasquez-Garcia, A. Akinwande, and M. Martinez-Sanchez, J. Microelectromech. Syst. **15**, 1272 (2006).
[47]E. Petro, A. Bruno, P. Lozano, L. E. Perna, and D. Freeman, in *AIAA Propulsion and Energy 2020 Forum* (American Institute of Aeronautics and Astronautics, 2020), p. 3612.
[48]J. Asher, Z. Huang, C. Cui, and J. Wang, J. Appl. Phys. **131**, 014902 (2022).
[49]J. S. Asher and J. Wang, J. Propul. Power **38**, 573 (2022).
[50]N. Nuwal, V. A. Azevedo, M. R. Klosterman, S. Budaraju, D. Levin, and J. Rovey, J. Appl. Phys. **130**, 184903 (2021).
[51]E. M. Petro, X. Gallud, S. K. Hampl, M. Schroeder, C. Geiger, and P. C. Lozano, J. Appl. Phys. **131**, 193301 (2022).
[52]C. B. Whittaker and B. A. Jorns, in *AIAA SciTech 2023 Forum* (American Institute of Aeronautics and Astronautics, 2023), p. 0041.
[53]O. Jia-Richards and P. C. Lozano, in *43rd IEEE Aerospace Conference* (Institute of Electrical and Electronics Engineers, 2022), pp. 1–8.
[54]A. Gorodetsky, C. B. Whittaker, A. Szulman, and B. Jorns, in *AIAA Propulsion and Energy 2021 Forum* (American Institute of Aeronautics and Astronautics, 2021), p. 3422.